

# OPTiML: Dense Semantic Invariance Using Optimal Transport for Self-Supervised Medical Image Representation

Azad Singh , Vandan Gorade and Deepak Mishra,

**Abstract**—Self-supervised learning (SSL) has emerged as a promising technique for medical image analysis due to its ability to learn without annotations. However, despite the promising potential, conventional SSL methods encounter limitations, including challenges in achieving semantic alignment and capturing subtle details. This leads to suboptimal representations, which fail to accurately capture the underlying anatomical structures and pathological details. In response to these constraints, we introduce a novel SSL framework OPTiML, employing optimal transport (OT), to capture the dense semantic invariance and fine-grained details, thereby enhancing the overall effectiveness of SSL in medical image representation learning. The core idea is to integrate OT with a cross-viewpoint semantics infusion module (CV-SIM), which effectively captures complex fine-grained details inherent in medical images across different viewpoints. In addition to the CV-SIM module, OPTiML imposes the variance and covariance regularizations within OT framework to force the model focus on clinically relevant information while discarding less informative features. Through these, the proposed framework demonstrates its capacity to learn semantically rich representations that can be applied to various medical imaging tasks. To validate its effectiveness, we conduct experimental studies on three publically available datasets from chest X-ray modality. Our empirical results reveal OPTiML’s superiority over state-of-the-art methods, across all evaluated tasks.

**Index Terms**—Self-supervised learning, Medical image analysis, Chest X-ray, Representation learning, Optimal Transport

## I. INTRODUCTION

Self-supervised learning (SSL) has gained significant momentum in the field of deep learning over the recent years [1]–[5]. In the medical image analysis domain, where large-scale annotated datasets are challenging to obtain, SSL is particularly useful due to its ability to harness unlabeled data [6]–[8]. However, conventional SSL methods, like SimCLR [2], MoCo [7], BYOL [4], Barlow-Twins [3], etc., though effective in various domains, encounter challenges when applied to the subtle complexities of medical images. The interpretation of medical images necessitates the deep understanding of both anatomical structures and pathological indicators for precise diagnosis and treatment decisions. This requirement poses a significant challenge for SSL methods that focus on general feature learning, while, often ignoring the fine-grained details and clinically relevant patterns [8]–[12].

Conventional SSL methods treat the entire image as a collection of isolated features, thereby missing out on the context and spatial dependencies between different anatomical regions. Moreover, the fine-grained variations in medical images

are particularly useful due to the coexistence of anatomical heterogeneity and the visual similarity of different regions. Heterogeneity pertains to the visual distinctions between instances of the same disease or anatomical structures [13]. For instance, the shape and size of a nodule may vary based on its stage and location. Conversely, visual similarity refers to the challenges in distinguishing between different diseases or structures that share common visual characteristics [14]. For instance, consolidation and pneumonia are labeled separately even though they are the types of lung opacities and have a natural relation. In context of SSL for medical applications it becomes imperative for models to adeptly capture these subtle variations. Failure to do so may result in trivial solutions and hinder the acquisition of a representative feature space, essential for meaningful medical image analysis [15], [16].

In addressing these challenges, the concept of dense semantic invariance holds potential to improve SSL for medical image analysis. It empowers the model to capture precise anatomical and pathological attributes, regardless of differences in viewpoints, orientations, and imaging conditions. In this context, we propose OPTiML, a novel solution that integrates concepts from SSL and optimal transport (OT) [17] to foster dense semantic invariance in medical image representation learning. The application of OT, provides a robust mechanism to measure the dissimilarity between representations and to find an optimal mapping between them. Additionally, OPTiML incorporates the cross-viewpoint semantics infusion module (CV-SIM) to enhance the model’s capability in capturing fine details from diverse viewpoints, thereby improving the alignment of semantically relevant features. Furthermore, to ensure that the acquired representations are both informative and less redundant, we apply variance and covariance regularizations [18] during the representation learning process. By incorporating variance regularization, OPTiML ensures stability in the learned representations, preventing the model from overemphasizing noise and irrelevant features. Concurrently, covariance regularization helps in preserving relationships and dependencies between different features within the images. This is particularly beneficial for capturing the intricate spatial and contextual relationships among anatomical structures or pathological patterns. The integration of variance and covariance regularizations within the OT framework enhances the ability of model to generate stable and semantically aligned representations.

The overall contributions of this paper are summarized as follows:

- OPTiML introduces an integration of OT into the SSL framework to achieve dense semantic invariance in medical image representations.
- OPTiML incorporates a novel CV-SIM module, which enhances the model’s ability to capture fine details from diverse viewpoints, thereby contributing to a more comprehensive and accurate representations.
- We evaluate the performance of OPTiML on diverse chest X-ray datasets, including NIH-Chest X-ray14, Vinbig-CXR, and RSNA. The results highlight effectiveness of the proposed model with consistent performance improvements across various medical imaging tasks.

In the subsequent sections of this paper, we provide a detailed exposition of the components of the OPTiML framework, elucidate the theoretical underpinnings of the CV-SIM module, delve into the OT application in the context of medical image representation, and present the comprehensive experimental analysis that validates the efficacy of our approach.

## II. BACKGROUND AND RELATED WORKS

**Self-supervised Learning.** The current SSL approaches employ a joint embedding architecture to acquire representations that are invariant to diverse perspectives [2], [4], [18]. These techniques have varying ways of circumventing the collapse of solutions. Negative sampling is employed by contrastive methods [1], [2], [6], [7] to push dissimilar samples apart from each other while clustering methods such as proposed in [19] ensure an equitable distribution of samples within clusters. Non-contrastive techniques [2]–[4], [18], [20], which serve as the alternative of contrastive methods, maintain the representations’ information content either by adopting architectural constraints such as asymmetric network, momentum encoder, stop-gradient, etc. or by applying specific regularization [3], [18]. Unlike the aforementioned global methods, local methods concentrate on learning a group of local features that describe smaller segments of an image. For instance, in [21] authors addressed the challenge of pixel-level self-supervised representation learning, crucial for tasks like object detection and semantic segmentation by leveraging pixel-level contrastive learning. Similarly DenseCL [22], a novel dense contrastive learning paradigm, introduced pixel-level SSL using a dense projection head and dense contrastive loss.

**SSL for Medical Image Analysis.** SSL has become an increasingly popular approach for medical image analysis [23]. A majority of recent works have shown the effectiveness of SSL for tasks such as segmentation, classification, and localization [6], [7], [24], [25]. The adoption of SSL techniques has predominantly leaned towards the utilization of contrastive learning approaches. However, in stark contrast, the number of approaches embracing non-contrastive SSL within this domain remains notably limited. For instance in [26],

authors introduced CheSS, a publicly accessible model pre-trained with 4.8-M chest X-ray images through contrastive learning on a large dataset. In [8], the authors presented a distinct SSL approach termed Multi-Instance Contrastive Learning (MICLe), which harnesses the multiple studies of the subject to create positive pairs. In another study [27], authors proposed a collaborative SSL framework DiRA that unites discriminative, restorative, and adversarial learning to learn fine-grained representations. MedAug [6] and PaCL [12] are another works based upon the contrastive approach that incorporates insightful metadata for selective positive and negative pairs. PCRL [28], [29], another contrastive approach, that enhances medical image representations by dynamically reconstructing diverse image contexts. This approach is applicable to both X-ray and CT modalities.

**Optimal Transport Theory.** OT determines the most efficient way to transform one distribution into another, considering the associated costs or distances between individual elements in the distributions [30]. It is popular for computer vision tasks like domain adaptation [31], multitask learning [32], feature matching [33], generative model [34] etc. where measuring dissimilarity or similarity between distributions is essential. Zheng *et al.* [35] framed label assignment in object detection, as an OT problem where the unit transportation cost between anchor and ground-truth pairs was defined by weighted summation of classification and regression losses, solved through Sinkhorn-Knopp Iteration for optimal assignment. Kim *et al.* proposed an identity-invariant facial expression recognition method using OT to quantify inter-identity variation, for optimal matching of similar expressions across different identities [36]. Zhu *et al.* introduced OT-guided translation network for unpaired image-to-image translation scheme to enhance retinal color fundus photography [37]. CUI *et al.* in [38] leveraged OT for nearest neighbor retrieval in on whole slide images (WSIs) to address performance degradation in multiple instance learning models when tested on out-of-domain data. OT has limited applicability in the medical domain due to complexities inherent in medical image data structures. In this work, we introduce a novel integration of OT within the SSL framework to enhance the effectively handle the medical image tasks.

## III. PROPOSED METHOD

In this section we first present preliminaries on OT theory, subsequently describe the proposed SSL framework OPTiML which comprises of two main stages: 1) formulation of dense semantic invariance as an OT problem and 2) cross-viewpoint semantics infusion module (CV-SIM).

**OPTiML SSL Framework.** OT has recently gained interest in computer vision applications which involve comparison of the images. By determining the optimal transportation plan between two images, we can quantify the similarity or dissimilarity between them in a way that considers the spatial arrangement of pixel intensities. This is particularly

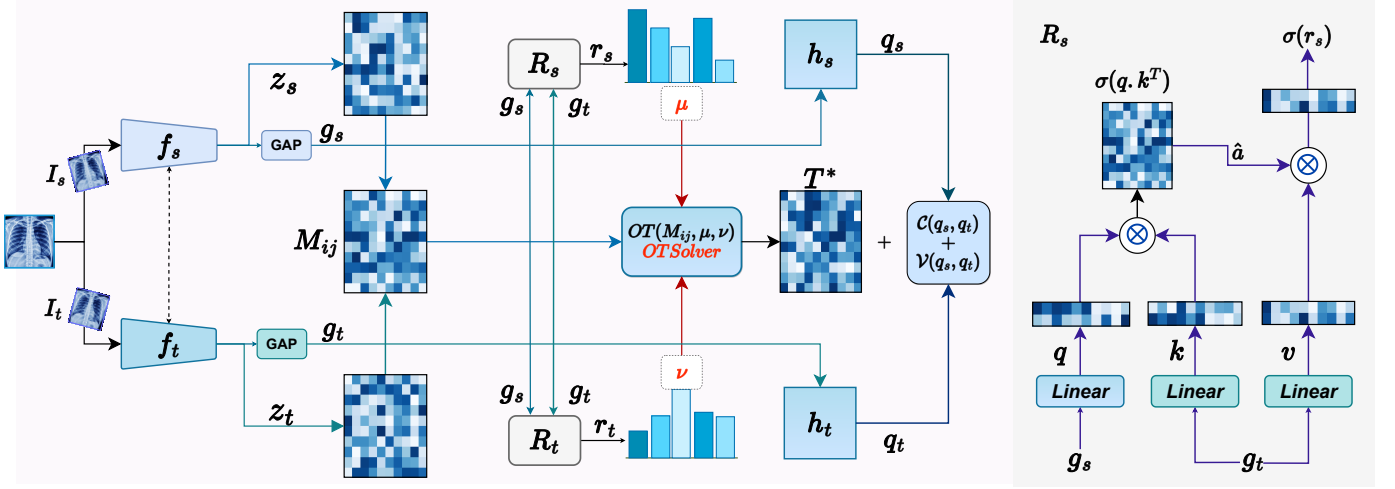


Fig. 1: Architecture of the OPTiML Framework.  $I_s$  and  $I_t$  are two augmented versions of  $I$ , pass through backbone encoders  $f_s$  and  $f_t$  to obtain  $z_s$  and  $z_t$  which OT solver subsequently utilizes along with the cost matrix  $M$ .  $g_s$  and  $g_t$  are the feature vectors after the global average pooling (GAP) layer which are expanded to  $q_s$  and  $q_t$ , to increase representational variability.

useful in applications like medical images where the pixel-wise differences may not capture perceptual similarity.

In this work we adapt OT in SSL to measure the optimal distance between two sets of image features which represent the embeddings extracted from each image. The primary objective is to ascertain the optimal flow of information between source and target images while ensuring the minimum associated cost in terms of distance between features. More specifically, as illustrated in Figure 1 OPTiML framework generates two augmented versions ( $I_s$  and  $I_t$ ) of the original input image  $I$  by applying random augmentations  $t_s$  and  $t_t$  sampled from a predefined set of augmentations  $\mathcal{T}$ .  $I_s$  and  $I_t$  undergo processing through two weight-shared CNN encoders  $f_s$  and  $f_t$ . The output of  $f_s$  and  $f_t$  are the dense feature maps  $z_s \in \mathbb{R}^{d \times hw}$  and  $z_t \in \mathbb{R}^{d \times hw}$  respectively, where  $d$  represents the number of channels while  $hw$  captures the spatial dimensions. Subsequently  $z_s$  and  $z_t$  are utilized to compute the discrepancy matrix  $C_{ij} \in \mathbb{R}^{d \times d}$ , where each element quantifies the cosine similarity between feature vectors at position  $i$  in  $z_s$  and the feature vector at position  $j$  in  $z_t$ . The discrepancy matrix  $C_{ij}$  is constructed as follows:

$$C_{ij} = \frac{z_s^T \cdot z_t}{\|z_s\| \|z_t\|} \quad (1)$$

Dense feature maps  $z_s$  and  $z_t$  offer advantage over post-pooling feature vectors for semantic alignment, as they preserve the spatial information and relationships between pixels in the original image. This enables the model to learn more meaningful representations for medical image applications, where the spatial arrangement of structures is vital for accurate diagnosis. The formulation of the OT problem aligns seamlessly with dense feature maps  $z_s$  and  $z_t$ , allowing for a more granular and accurate estimation of the cost associated with transferring of information between corresponding positions.

Furthermore,  $z_s$  and  $z_t$  undergo a global average pooling layer  $GAP$  to output  $g_s$  and  $g_t$ , that condenses the spatial information captured by the dense feature maps, into single-dimensional compact representations. Subsequently,  $g_s$  and  $g_t$ , are projected to an high dimensional space using  $MLP$  expansion heads  $h_s$  and  $h_t$  to output  $q_s$  and  $q_t$  respectively.  $g_s$  and  $g_t$  are further utilized by the CV-SIM modules  $R_s$  and  $R_t$  in each branch of the network. The subsequent section provides the details of the CV-SIM.

**Cross-Viewpoint Semantics Infusion Module.** CV-SIM module incorporates, multi-head cross-view attention mechanism, where each head attends to diverse subspaces of queries and keys. This contributes in navigating the high-dimensional feature space to extract subtle relationships and dependencies across different viewpoints within the data. In this context, it linearly transform  $g_s$  into  $q$  and  $g_t$  into  $k$  and  $v$ , each having a dimension of  $\mathbb{R}^d$ . Subsequently, a multi-head attention mechanism computes attention scores  $\hat{a}$  through a scaled dot-product between queries ( $q$ ) and keys ( $k$ ) by employing  $\sigma(\frac{q \cdot k^T}{\sqrt{dim}})$ .  $\sigma$  represents the softmax function, which transforms relevance attention scores into attention weights while  $dim$  denotes the dimensionality of the query and key vector.

Subsequently, CV-SIM, further refines the representation by computing the attended values, through a weighted sum operation, where the attention weights guide the aggregation of information from the target representation  $v$  based on the computed attention weights  $\hat{a}$ . This, ensures that CV-SIM captures intricate dependencies across different viewpoints, contributing to the enrichment of the overall feature space. The attended values computation yields an enhanced representation  $r_s \in \mathbb{R}^d$ . Likewise, a corresponding procedure is executed in  $R_t$ , where the roles of  $g_s$  and  $g_t$  are interchanged to generate the corresponding outcome  $r_t \in \mathbb{R}^d$ . The resulting enhanced representations  $r_s$  and  $r_t$  from  $R_s$  and  $R_t$  respectively, un-

dergoes another transformation through the softmax function to convert it into a probabilistic distribution  $\mu$  and  $\nu$  over the visual feature spaces respectively. OT solver utilized these  $\mu$  and  $\nu$  as the marginal constraints of the transport plan such that the total cost of transporting features from one image to another is minimum. This step ensures that the probability distribution derived from the refined representation is effectively incorporated into the optimization process facilitated by the OT solver, contributing to the alignment of features across different branches within the OPTiML framework.

**Modelling Dense Semantic Invariance as OT Problem.** In OPTiML framework, we cast challenge of achieving dense semantic invariance between  $I_s$  and  $I_t$  as an OT problem by employing a matrix  $T$  representing the matching distribution of features across different viewpoints. The goal is to maximize semantic invariance across  $I_s$  and  $I_t$  by obtaining a global optimal transport plan  $T^*$ . To formulate the optimization problem, we define the total discrepancy as  $\sum_{ij} T_{ij} C_{ij}$  where  $C_{ij}$  is the cosine similarity-based discrepancy matrix computed from the dense feature  $z_s$  and  $z_t$ . In order to find  $T^*$ , that maximizes this total discrepancy to ensure effective alignment of semantic features, we define the cost matrix  $M_{ij} = 1 - C_{ij}$  which we need to minimize. To avoid the trivial solutions we introduce probability distributions  $\mu$  and  $\nu$  in the CV-SIM of the OPTiML framework. Note that in the CV-SIM module,  $\mu$  and  $\nu$  are not simply initialized as uniform distributions, which is a common practice, but instead, these are computed using the intra- and inter-relational information. This means that  $\mu$  and  $\nu$  encode task-specific information while giving less weight to the irrelevant dimensions. The OT problem is then formulated as:

$$T^* = \arg \min_{T \in \Pi(\mu, \nu)} \sum_{i=1}^d \sum_{j=1}^d T_{ij} M_{ij} = \min_T \langle T, M \rangle \quad (2)$$

where  $\Pi(\mu, \nu)$  represents the set of transport plans subjected to  $T \in \mathbb{R}_+^{d \times d} : T\mathbf{1} = \mu, T^\top \mathbf{1} = \nu$ . The constraints  $T\mathbf{1} = \mu$  and  $T^\top \mathbf{1} = \nu$  enforce the conservation of mass where  $\mathbf{1}$  denotes a vector of ones.  $T_{ij}$  is the amount of mass moved from  $i^{th}$  point in  $\mu$  to  $j^{th}$  point in  $\nu$  to achieve minimal cost. The optimization process formulated in equation (2) seeks to determine the optimal transport plan  $T^*$  that minimizes the total matching difference subjected to prescribed marginal constraints. Equation (2) can be efficiently solved using Sinkhorn algorithm [39], [40], which makes it compatible with the deep learning framework.  $T^*$  is subsequently used to obtain the OT loss term for the final objective as  $L_{OT} = \langle T^*, M \rangle$ .

Further, inspired by VICReg [18], we employ two regularization terms: Variance (*var*) and Covariance (*cov*), using  $q_s$  and  $q_t$  independently in both branches of the model's architecture mainly to avoid any possibility of collapse. The final objective for OPTiML is formulated in Eq. (3), where  $\alpha$ ,  $\beta$ , and  $\eta$ , are hyperparameters.

$$L_{MT} = \alpha \times L_{OT} + \beta \times [\text{var}(q_s) + \text{var}(q_t)] + \eta \times [\text{cov}(q_s) + \text{cov}(q_t)] \quad (3)$$

By iteratively refining the representations through CV-SIM and aligning them using OT, the method establishes a mechanism that inherently promotes dense semantic invariance while fostering view-invariant features. The result is a set of representations that capture not only the details specific to each view but also the essential semantic content that is consistent across views.

#### IV. EXPERIMENTAL PLATFORM

**Datasets.** The proposed approach employs SSL pre-training using publicly available NIH Chest X-ray [41] dataset which has 112,120 chest X-ray images labeled with 14 thoracic pathologies. Further, for evaluations of the learned representations we use VinBig-CXR [42] and RSNA Pneumonia [43] datasets along with the NIH dataset. VinBig-CXR contains 18K chest X-ray images, annotated into 14 pathologies. The RSNA [43] dataset consists of 30k chest radiographs captured from a frontal view, each annotated as either healthy or pneumonia. We also perform segmentation as the downstream evaluation on SIIM-ACR Pneumothorax [44] data.

**Evaluation Protocols** To assess the efficacy of the learned representations, we conduct downstream tasks involving chest X-ray image classification and segmentation using only the backbone encoder  $f_s$  obtained from pre-training. Following the established practices in the literature [2], [4], [18], [29], we adopted two distinct evaluation protocols (1) frozen and (2) fine-tuning for which we add a single linear layer classifier on top of the pretrained backbone encoder. In the frozen evaluation protocol, the parameters of the backbone CNN encoder remain fixed, ensuring that only the linear layer's parameters are updated during downstream training. Conversely, in the fine-tuning evaluation protocol, we fine-tuned both the SSL pretrained backbone CNN encoder and the newly added linear classifier layer. We presented results on the test/validation dataset using various subsets (1%, 10%, and All) of the training data. We perform the segmentation under fine-tuning evaluation protocol using Resnet based U-Net architecture after updating the encoder's parameter with that obtained from OPTiML's pretraining.

**Method Compared.** For comparison, the baselines encompassed both supervised, including initialization with random (Sup.1) and ImageNet (Sup.2) weights, and a range of SOTA SSL techniques. In the SSL domain, we included as SimCLR [2], MoCov2 [1], BYOL [4], SimSiam [45], VICReg [18] and PCRLv2 [29]. We perform the pretraining for these baselines ourselves, following their official implementations and keeping alignment with our proposed approach's training protocol.

**Implementation Details** We utilize ResNet18 as the backbone encoder for SSL pretraining. The training of the encoder involves a batch size of 64 over a span of 300 epochs. The output of the encoder is then propagated through an MLP head serving as an expander. This expander head comprises three linear layers, each featuring a dimensionality of 2048, and

TABLE I: Comparison of the considered approaches under the semi-supervised linear evaluation protocol for the classification task on NIH, Vinbig-CXR and RSNA datasets, after finetuning the representations using different subsets of labeled samples from training set. The arrows  $\uparrow$  and  $\downarrow$  indicate improvement and decrement compared with bs.

Methods	NIH			VinBig-CXR			RSNA		
	1%	10%	100%	1%	10%	100%	1%	10%	100%
Sup.1	61.0 <sub>(-6.8)</sub> $\downarrow$	71.1 <sub>(-3.5)</sub> $\downarrow$	76.8 <sub>(-4.1)</sub> $\downarrow$	71.1 <sub>(-8.7)</sub> $\downarrow$	85.0 <sub>(-3.3)</sub> $\downarrow$	91.0 <sub>(-2.4)</sub> $\downarrow$	77.0 <sub>(-1.9)</sub> $\downarrow$	79.8 <sub>(-1.1)</sub> $\downarrow$	80.0 <sub>(-3.1)</sub> $\downarrow$
Sup.2 <sub>(bs)</sub>	67.8 <sub>(0.0)</sub>	74.6 <sub>(0.0)</sub>	80.9 <sub>(0.0)</sub>	79.8 <sub>(0.0)</sub>	88.3 <sub>(0.0)</sub>	93.4 <sub>(0.0)</sub>	78.9 <sub>(0.0)</sub>	80.9 <sub>(0.0)</sub>	83.1 <sub>(0.0)</sub>
SimCLR	67.1 <sub>(-0.7)</sub> $\downarrow$	74.8 <sub>(1.3)</sub> $\uparrow$	78.9 <sub>(-0.2)</sub> $\downarrow$	77.9 <sub>(2.0)</sub> $\uparrow$	87.7 <sub>(-0.6)</sub> $\downarrow$	92.4 <sub>(1.9)</sub> $\uparrow$	80.0 <sub>(0.9)</sub> $\uparrow$	81.1 <sub>(1.0)</sub> $\uparrow$	81.8 <sub>(0.7)</sub> $\uparrow$
MoCoV2	66.8 <sub>(-1.0)</sub> $\downarrow$	74.6 <sub>(0.0)</sub> $\downarrow$	79.4 <sub>(-0.5)</sub> $\downarrow$	77.1 <sub>(1.1)</sub> $\uparrow$	86.2 <sub>(-2.1)</sub> $\downarrow$	92.0 <sub>(0.9)</sub> $\uparrow$	79.4 <sub>(-0.5)</sub> $\downarrow$	81.3 <sub>(-0.4)</sub> $\downarrow$	82.0 <sub>(-0.9)</sub> $\downarrow$
DenseCL	67.7 <sub>(-0.1)</sub> $\downarrow$	76.4 <sub>(1.8)</sub> $\uparrow$	81.4 <sub>(0.5)</sub> $\uparrow$	82.7 <sub>(3.0)</sub> $\uparrow$	88.7 <sub>(-0.3)</sub> $\downarrow$	93.9 <sub>(1.5)</sub> $\uparrow$	79.9 <sub>(1.0)</sub> $\uparrow$	81.1 <sub>(1.8)</sub> $\uparrow$	82.3 <sub>(1.1)</sub> $\uparrow$
BYOL	66.3 <sub>(-0.8)</sub> $\downarrow$	74.5 <sub>(-2.1)</sub> $\downarrow$	78.8 <sub>(-2.1)</sub> $\downarrow$	76.2 <sub>(-1.7)</sub> $\downarrow$	85.8 <sub>(-3.3)</sub> $\downarrow$	85.9 <sub>(-4.2)</sub> $\downarrow$	78.3 <sub>(-1.0)</sub> $\downarrow$	80.5 <sub>(-0.9)</sub> $\downarrow$	82.5 <sub>(-1.1)</sub> $\downarrow$
SimSiam	66.6 <sub>(-0.5)</sub> $\downarrow$	74.3 <sub>(-2.1)</sub> $\downarrow$	78.5 <sub>(-2.4)</sub> $\downarrow$	75.8 <sub>(-1.9)</sub> $\downarrow$	85.9 <sub>(-3.1)</sub> $\downarrow$	91.5 <sub>(0.1)</sub> $\uparrow$	78.1 <sub>(-0.8)</sub> $\downarrow$	80.1 <sub>(-0.8)</sub> $\downarrow$	82.1 <sub>(-1.0)</sub> $\downarrow$
VICReg	67.4 <sub>(0.3)</sub> $\uparrow$	75.5 <sub>(0.9)</sub> $\uparrow$	80.2 <sub>(1.3)</sub> $\uparrow$	76.9 <sub>(-1.0)</sub> $\downarrow$	87.5 <sub>(0.8)</sub> $\uparrow$	91.9 <sub>(0.5)</sub> $\uparrow$	79.5 <sub>(0.6)</sub> $\uparrow$	80.7 <sub>(0.2)</sub> $\uparrow$	82.7 <sub>(0.4)</sub> $\uparrow$
PCRLv2	67.5 <sub>(0.2)</sub> $\uparrow$	75.6 <sub>(0.9)</sub> $\uparrow$	81.0 <sub>(2.5)</sub> $\uparrow$	75.9 <sub>(-2.0)</sub> $\downarrow$	87.8 <sub>(0.1)</sub> $\downarrow$	93.4 <sub>(1.5)</sub> $\uparrow$	80.1 <sub>(0.7)</sub> $\uparrow$	81.5 <sub>(1.0)</sub> $\uparrow$	82.9 <sub>(0.9)</sub> $\uparrow$
<b>OPTiML</b>	<b>68.8<sub>(1.0)</sub><math>\uparrow</math></b>	<b>77.6<sub>(3.0)</sub><math>\uparrow</math></b>	<b>82.5<sub>(1.6)</sub><math>\uparrow</math></b>	<b>83.8<sub>(4.0)</sub><math>\uparrow</math></b>	<b>89.5<sub>(1.2)</sub><math>\uparrow</math></b>	<b>94.6<sub>(1.2)</sub><math>\uparrow</math></b>	<b>81.4<sub>(2.5)</sub><math>\uparrow</math></b>	<b>82.3<sub>(1.4)</sub><math>\uparrow</math></b>	<b>84.0<sub>(0.9)</sub><math>\uparrow</math></b>

is accompanied by ReLU activation and batch normalization within each layer. The optimization strategy employed is the LARS optimization algorithm, with a learning rate of  $3e-4$  and a weight decay of  $1e-4$ . The values of  $\beta$  and  $\eta$  are directly adopted from VICReg [18], while  $\alpha$  is empirically set to 0.6 for optimal performance.

#### A. Results and Analysis

This section presents the evaluation results of the proposed framework under following evaluation protocols.

1) *Quantitative Results under Finetuning Protocol*: Table I presents the evaluation results from the test set on the downstream classification task under liner probing with fine-tuning using subsets (1%, 10% and 100%) of labeled data from the train set. OPTiML consistently outperforms the baselines across all the evaluated tasks. Notably, for the 1% subset of labeled data from NIH, OPTiML stands out by achieving highest AUC score of 0.688. On increasing the labeled data to 10% OPTiML persists superiority with an average performance gain of 2% over baseline methods. When considered whole training data for finetuning, the proposed SSL framework outperforms all the SOTA SSL and supervised baseline methods including PCRLv2 which is specifically designed for medical image analysis,

**Transferability to other datasets** In the context of transfer learning, OPTiML consistently exhibits performance gain for the VinBig-CXR dataset. The performance gain indicates OPTiML’s ability to learn generalized representations, demonstrating its potential for transfer learning scenarios, where labeled samples are limited. Similar trends are observed for RSNA dataset, for which also, OPTiML outperforms all the SOTA SSL and supervised baselines by reaching to highest AUC score of 0.840. This improvement over baseline methods highlights OPTiML’s capacity to extract discriminative features that contribute to enhanced classification performance. The transferability of learned representations is particularly crucial in medical imaging applications where adapting models to new datasets or tasks is common and OPTiML’s perfor-

mance gains on different datasets, highlights its effectiveness in capturing versatile and transferable representations.

#### 2) Quantitative Results under Linear Evaluation(Frozen):

Table II reports the linear evaluation results on various datasets and subsets under frozen settings. In the case of the NIH Chest X-ray dataset, OPTiML consistently outperforms the baselines across different subsets, achieving an AUC score of 0.638 for 1% labeled data. Similar trends are observed when labeled data increases to 10% and when considered the whole data for which OPTiML obtain highest AUC score of 0.739 by outperforming all the baseline methods. Similarly, on the Vinbig-CXR dataset, OPTiML excels across all subsets, attaining the highest AUC of 0.781 for the 10% subset. However, for 1% subset, MoCoV2 exceptionally outperforms the proposed approach. For the RSNA dataset also, OPTiML continue to perform better than the considered baseline methods. This reinforces its efficiency as a feature extractor in transfer learning scenarios, where efficient use of resources is a crucial consideration.

3) *Qualitative Results*: Figure 2 illustrates diagnostic heatmaps generate from OPTiML and SSL baseline methods, serve as as visual representations of model interpretations for chest X-ray images that have undergone fine-tuning with 1% of training samples from the NIH dataset. The heatmaps highlight regions within the chest X-ray images that are considered significant by the respective models for diagnostic purposes. By comparing the diagnostic heatmaps generated we observe OPTiML outperforms baseline SSL methods in terms of highlighting regions identified by ground truth, as indicated by the bounding boxes. By comparing these heatmaps to the ground truth bounding boxes, it becomes evident that OPTiML provides more accurate and precise localization of relevant regions within the chest X-ray images. The accurate alignment between ground truth and highlighted regions in OPTiML’s heatmap demonstrate its effectiveness in capturing and emphasizing diagnostically significant regions, showcasing its ability to leverage SSL for improved interpretability in medical image analysis.



TABLE II: Linear Evaluation on different datasets and subsets under frozen settings. The table compares the proposed method and baselines across NIH Chest X-ray, Vinbig-CXR, and RSNA datasets.

Methods	NIH			Vinbig-CXR			RSNA		
	1%	10%	All	1%	10%	All	1%	10%	All
Sup.1	56.6 <sub>(-6.0)</sub> ↓	59.1 <sub>(-9.2)</sub> ↓	61.8 <sub>(-10.8)</sub> ↓	56.8 <sub>(-0.6)</sub> ↓	59.4 <sub>(-16.8)</sub> ↓	71.1 <sub>(-13.9)</sub> ↓	75.7 <sub>(-10.8)</sub> ↓	76.8 <sub>(0.0)</sub>	78.2 <sub>(0.0)</sub>
Sup.2 <sub>(bs)</sub>	62.6 <sub>(0.0)</sub>	68.3 <sub>(0.0)</sub>	72.8 <sub>(0.0)</sub>	57.4 <sub>(0.0)</sub>	76.2 <sub>(0.0)</sub>	85.1 <sub>(0.0)</sub>	85.7 <sub>(0.0)</sub>	76.8 <sub>(0.0)</sub>	78.2 <sub>(0.0)</sub>
SimCLR	62.4 <sub>(-0.2)</sub> ↓	68.3 <sub>(0.0)</sub>	73.0 <sub>(0.2)</sub> ↑	66.3 <sub>(8.9)</sub> ↑	77.4 <sub>(1.2)</sub> ↑	85.3 <sub>(0.2)</sub> ↑	76.9 <sub>(8.8)</sub> ↑	78.9 <sub>(2.1)</sub> ↑	81.8 <sub>(3.6)</sub> ↑
MoCov2	61.9 <sub>(-0.7)</sub> ↓	68.9 <sub>(0.6)</sub> ↑	72.6 <sub>(-0.2)</sub> ↓	66.7 <sub>(0.4)</sub> ↑	74.6 <sub>(2.8)</sub> ↑	85.5 <sub>(0.4)</sub> ↑	76.8 <sub>(1.1)</sub> ↑	78.1 <sub>(1.3)</sub> ↑	81.2 <sub>(3.0)</sub> ↑
DenseCL	62.9 <sub>(0.3)</sub> ↑	69.5 <sub>(0.6)</sub> ↑	72.7 <sub>(-0.1)</sub> ↓	64.3 <sub>(-1.4)</sub> ↓	73.6 <sub>(0.2)</sub> ↑	85.5 <sub>(0.0)</sub>	76.8 <sub>(1.0)</sub> ↑	78.8 <sub>(0.7)</sub> ↑	81.2 <sub>(0.0)</sub>
BYOL	61.7 <sub>(-0.9)</sub> ↓	65.8 <sub>(-3.1)</sub> ↓	69.9 <sub>(-2.9)</sub> ↓	65.6 <sub>(-1.1)</sub> ↓	77.8 <sub>(0.4)</sub> ↑	84.0 <sub>(-1.1)</sub> ↓	76.5 <sub>(-0.3)</sub> ↓	78.4 <sub>(0.4)</sub> ↑	80.9 <sub>(2.3)</sub> ↑
SimSiam	62.0 <sub>(-0.6)</sub> ↓	65.9 <sub>(-2.4)</sub> ↓	69.8 <sub>(-3.0)</sub> ↓	65.0 <sub>(-8.8)</sub> ↓	77.5 <sub>(-6.3)</sub> ↓	84.1 <sub>(-0.8)</sub> ↓	76.2 <sub>(9.5)</sub> ↑	77.8 <sub>(1.0)</sub> ↑	80.5 <sub>(2.3)</sub> ↑
VicReg	62.7 <sub>(0.1)</sub> ↑	68.7 <sub>(0.4)</sub> ↑	72.3 <sub>(-0.5)</sub> ↓	65.3 <sub>(7.1)</sub> ↑	76.5 <sub>(0.3)</sub> ↑	83.2 <sub>(2.1)</sub> ↑	76.7 <sub>(0.8)</sub> ↑	78.4 <sub>(1.6)</sub> ↑	81.2 <sub>(2.4)</sub> ↑
PCRLv2	59.8 <sub>(-2.8)</sub> ↓	68.6 <sub>(0.3)</sub> ↑	72.9 <sub>(0.1)</sub> ↑	59.8 <sub>(2.4)</sub> ↑	71.9 <sub>(5.5)</sub> ↑	78.0 <sub>(6.9)</sub> ↑	76.8 <sub>(0.0)</sub>	80.3 <sub>(3.5)</sub> ↑	81.1 <sub>(2.9)</sub> ↑
OPTiML	<b>63.8<sub>(1.2)</sub>↑</b>	<b>70.3<sub>(2.0)</sub>↑</b>	<b>73.9<sub>(1.1)</sub>↑</b>	<b>66.1<sub>(8.7)</sub>↑</b>	<b>78.1<sub>(1.9)</sub>↑</b>	<b>86.5<sub>(1.4)</sub>↑</b>	<b>80.0<sub>(1.0)</sub>↑</b>	<b>81.3<sub>(4.5)</sub>↑</b>	<b>82.1<sub>(3.9)</sub>↑</b>

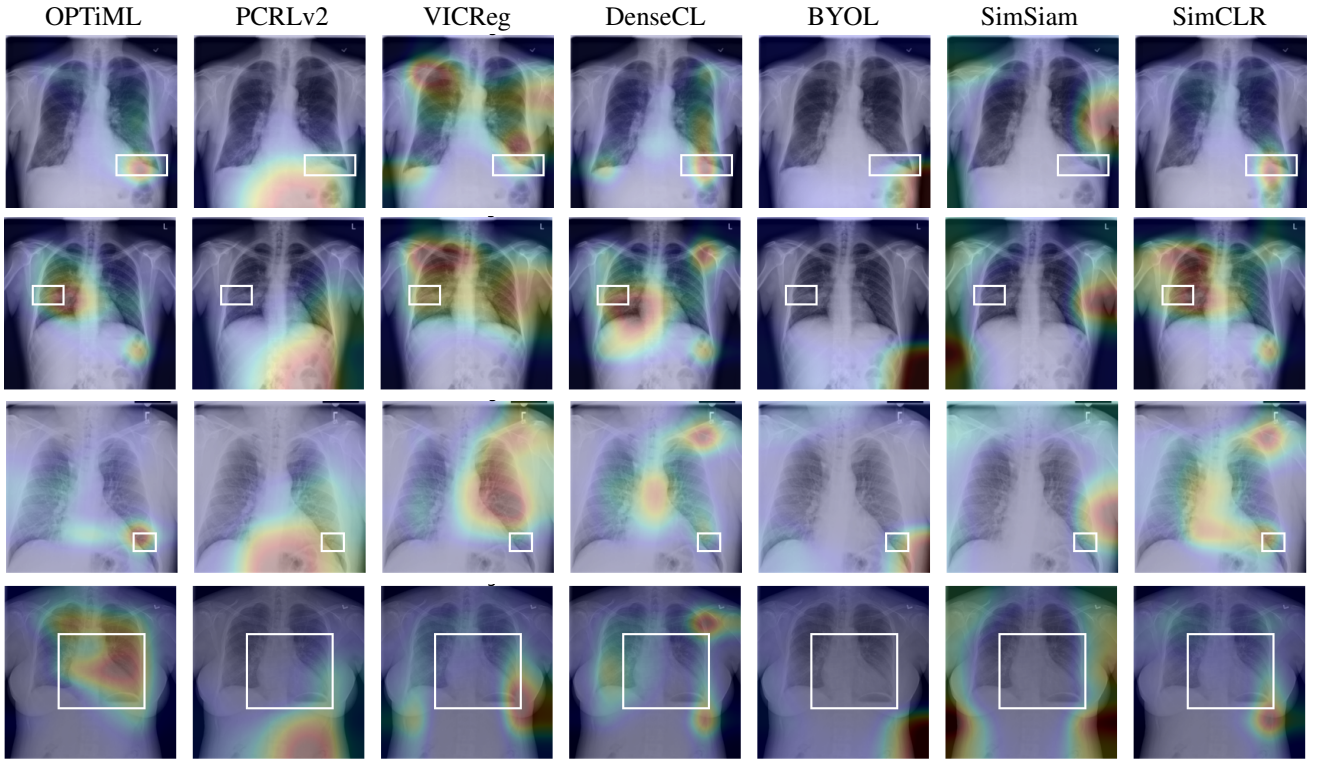


Fig. 2: Diagnostic heatmaps generated by OPTiML and the considered SSL baseline methods, represent interpretations of chest X-ray images fine-tuned with 1% of training samples from the NIH dataset.

**Transferability to Segmentation Task** Furthermore, we also measure the performance of OPTiML under the transfer learning regime for segmentation as the downstream task. For this, we consider the pneumothorax segmentation task on SIIM-ACR samples. Figure 3 presents the results for which we fine-tune a U-Net model which uses the backbone encoder initialized with the weights obtained from the OPTiML pre-training while the decoder is randomly initialized. The results in terms of dice coefficient demonstrate a comparatively better generalization ability and transferability of the representations produced by the OPTiML with highest dice score of 0.586. Results show that dense semantic invariance, employed in OPTiML, is more effective than the traditional invariance

approaches such as in the baseline SSL methods.

### B. Ablation Study

We conduct two studies to evaluate the effectiveness of different components of the OPTiML framework, across various data percentages on the NIH dataset and the observations are summarized in Table III.

1) *Effect of var and cov Regularizers.*: In this study, OPTiML is evaluated without the *var* and *cov* regularization components. The results indicate decline in performance, highlighting the importance of these regularization terms in preserving valuable information during the training process.

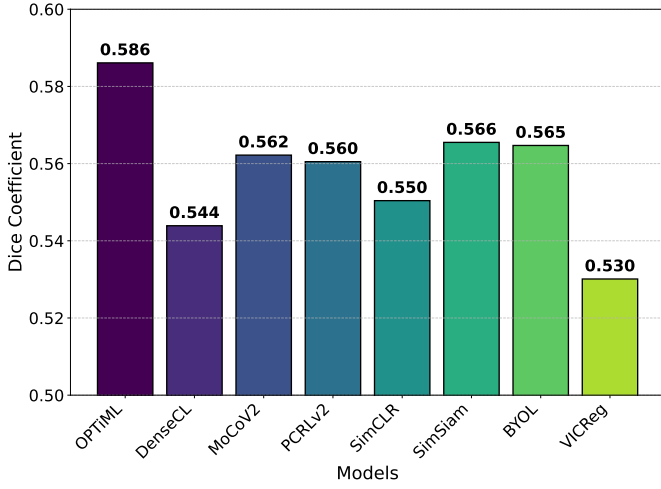


Fig. 3: Segmentation on SIIM-ACR Pneumothorax dataset obtained after finetuning the representations obtained from NIH pretraining.

TABLE III: Results of an ablation study conducted on OPTiML across various data percentages on the NIH dataset.

Method	var+cov	CV-SIM	1%	10%
OPTiML	✗	✓	0.679	0.765
	✓	✗	0.678	0.769
	✗	✗	0.673	0.762
	✓	✓	<b>0.685</b>	<b>0.776</b>

2) *Relevance of CV-SIM Module.*: This study involves assessing OPTiML without the CV-SIM. This module is an important part of OPTiML, enhancing the model’s ability to capture subtle dependencies across different viewpoints. The observed decrease in performance highlights its significance in maintaining and enriching the overall feature space.

Further, we discarded both *var* and *cov* regularization and the CV-SIM module from OPTiML. The combined absence of these components leads to a further decline in performance, emphasizing the cumulative impact of these elements on the overall effectiveness of the OPTiML framework. The results demonstrate that the optimal configuration, where both *var* and *cov* regularization and the CV-SIM module are included in OPTiML, yields the highest performance

## V. CONCLUSION

In this work we introduce OPTiML to enhance the capabilities of SSL framework. The proposed framework, demonstrate the effective integration of the OT in SSL to learn dense-semantic invariant features which are critical in medical images. We also proposed CV-SIM module to refine the dense semantic features from different viewpoints. Further, the incorporation of *var* and *cov* regularization terms are effective to maintain diversity and removing the redundancy. Through, experimental results we demonstrate that OPTiML identifies precise pathological regions relevant to the given task. These findings emphasize the importance of learning view invariant features by achieving

dense semantic invariance to align the representations in SSL framework.

## REFERENCES

- [1] X. Chen, H. Fan, R. Girshick, and K. He, “Improved baselines with momentum contrastive learning,” *arXiv preprint arXiv:2003.04297*, 2020.
- [2] T. Chen, S. Kornblith, M. Norouzi, and G. Hinton, “A simple framework for contrastive learning of visual representations,” 2020.
- [3] J. Zbontar, L. Jing, I. Misra, Y. LeCun, and S. Deny, “Barlow twins: Self-supervised learning via redundancy reduction,” 2021.
- [4] J.-B. Grill, F. Strub, F. Altché, C. Tallec, P. H. Richemond, E. Buchatskaya, C. Doersch, B. A. Pires, Z. D. Guo, M. G. Azar, B. Piot, K. Kavukcuoglu, R. Munos, and M. Valko, “Bootstrap your own latent: A new approach to self-supervised learning,” 2020.
- [5] V. Gorade, A. Singh, and D. Mishra, “Large scale time-series representation learning via simultaneous low-and high-frequency feature bootstrapping,” *IEEE Transactions on Neural Networks and Learning Systems*, 2023.
- [6] Y. N. T. Vu, R. Wang, N. Balachandar, C. Liu, A. Y. Ng, and P. Rajpurkar, “Medaug: Contrastive learning leveraging patient metadata improves representations for chest x-ray interpretation,” 2021.
- [7] H. Sowrirajan, J. Yang, A. Y. Ng, and P. Rajpurkar, “Moco-cxr: Moco pretraining improves representation and transferability of chest x-ray models,” 2021.
- [8] S. Azizi, B. Mustafa, F. Ryan, Z. Beaver, J. Freyberg, J. Deaton, A. Loh, A. Karthikesalingam, S. Kornblith, T. Chen, V. Natarajan, and M. Norouzi, “Big self-supervised models advance medical image classification,” 2021.
- [9] Z.-M. Chen, X.-S. Wei, P. Wang, and Y. Guo, “Multi-label image recognition with graph convolutional networks,” in *Proceedings of the IEEE/CVF conference on computer vision and pattern recognition*, 2019, pp. 5177–5186.
- [10] V. Gorade, S. Mittal, D. Jha, and U. Bagci, “Synergynet: Bridging the gap between discrete and continuous representations for precise medical image segmentation,” in *Proceedings of the IEEE/CVF Winter Conference on Applications of Computer Vision*, 2024, pp. 7768–7777.
- [11] T. N. Kipf and M. Welling, “Semi-supervised classification with graph convolutional networks,” *arXiv preprint arXiv:1609.02907*, 2016.
- [12] V. Gorade, S. Mittal, and R. Singhal, “Pacl: Patient-aware contrastive learning through metadata refinement for generalized early disease diagnosis,” *Computers in Biology and Medicine*, vol. 167, p. 107569, 2023.
- [13] M. Zheng, S. You, F. Wang, C. Qian, C. Zhang, X. Wang, and C. Xu, “Ressl: Relational self-supervised learning with weak augmentation,” *Advances in Neural Information Processing Systems*, vol. 34, pp. 2543–2555, 2021.
- [14] X. Xing, Y. Hou, H. Li, Y. Yuan, H. Li, and M. Q.-H. Meng, “Categorical relation-preserving contrastive knowledge distillation for medical image classification,” in *Medical Image Computing and Computer Assisted Intervention—MICCAI 2021: 24th International Conference, Strasbourg, France, September 27–October 1, 2021, Proceedings, Part V 24*. Springer, 2021, pp. 163–173.
- [15] X. Zhao, C. Fang, D.-J. Fan, X. Lin, F. Gao, and G. Li, “Cross-level contrastive learning and consistency constraint for semi-supervised medical image segmentation,” in *2022 IEEE 19th International Symposium on Biomedical Imaging (ISBI)*. IEEE, 2022, pp. 1–5.
- [16] S. Wang, B. Zhang, Y. Xu, Y. Wu, and B. Xiao, “Rcl: Relation contrastive learning for zero-shot relation extraction,” in *Findings of the Association for Computational Linguistics: NAACL 2022*, 2022, pp. 2456–2468.

- [17] G. Luise, A. Rudi, M. Pontil, and C. Ciliberto, "Differential properties of sinkhorn approximation for learning with wasserstein distance," *Advances in Neural Information Processing Systems*, vol. 31, 2018.
- [18] A. Bardes, J. Ponce, and Y. LeCun, "Vicreg: Variance-invariance-covariance regularization for self-supervised learning," 2022.
- [19] M. Caron, I. Misra, J. Mairal, P. Goyal, P. Bojanowski, and A. Joulin, "Unsupervised learning of visual features by contrasting cluster assignments," *Advances in Neural Information Processing Systems*, vol. 33, pp. 9912–9924, 2020.
- [20] M. Caron, H. Touvron, I. Misra, H. Jégou, J. Mairal, P. Bojanowski, and A. Joulin, "Emerging properties in self-supervised vision transformers," 2021.
- [21] Z. Xie, Y. Lin, Z. Zhang, Y. Cao, S. Lin, and H. Hu, "Propagate yourself: Exploring pixel-level consistency for unsupervised visual representation learning," in *Proceedings of the IEEE/CVF Conference on Computer Vision and Pattern Recognition*, 2021, pp. 16 684–16 693.
- [22] X. Wang, R. Zhang, C. Shen, T. Kong, and L. Li, "Dense contrastive learning for self-supervised visual pre-training," in *Proceedings of the IEEE/CVF Conference on Computer Vision and Pattern Recognition*, 2021, pp. 3024–3033.
- [23] S. Shurrab and R. Duwairi, "Self-supervised learning methods and applications in medical imaging analysis: A survey," *PeerJ Computer Science*, vol. 8, p. e1045, 2022.
- [24] C. Zhang and Y. Gu, "Dive into self-supervised learning for medical image analysis: Data, models and tasks," *arXiv preprint arXiv:2209.12157*, 2022.
- [25] Y. Huang, L. Lin, P. Cheng, J. Lyu, and X. Tang, "Lesion-based contrastive learning for diabetic retinopathy grading from fundus images," in *Medical Image Computing and Computer Assisted Intervention—MICCAI 2021: 24th International Conference, Strasbourg, France, September 27–October 1, 2021, Proceedings, Part II 24*. Springer, 2021, pp. 113–123.
- [26] K. Cho, K. D. Kim, Y. Nam, J. Jeong, J. Kim, C. Choi, S. Lee, J. S. Lee, S. Woo, G.-S. Hong *et al.*, "Chess: Chest x-ray pre-trained model via self-supervised contrastive learning," *Journal of Digital Imaging*, pp. 1–9, 2023.
- [27] F. Haghighi, M. R. H. Taher, M. B. Gotway, and J. Liang, "Dira: discriminative, restorative, and adversarial learning for self-supervised medical image analysis," in *Proceedings of the IEEE/CVF Conference on Computer Vision and Pattern Recognition*, 2022, pp. 20 824–20 834.
- [28] H.-Y. Zhou, C. Lu, S. Yang, X. Han, and Y. Yu, "Preservational learning improves self-supervised medical image models by reconstructing diverse contexts," in *Proceedings of the IEEE/CVF International Conference on Computer Vision*, 2021, pp. 3499–3509.
- [29] H.-Y. Zhou, C. Lu, C. Chen, S. Yang, and Y. Yu, "A unified visual information preservation framework for self-supervised pre-training in medical image analysis," *IEEE Transactions on Pattern Analysis and Machine Intelligence*, 2023.
- [30] L. Chen, D. Wang, Z. Gan, J. Liu, R. Hénao, and L. Carin, "Wasserstein contrastive representation distillation," in *Proceedings of the IEEE/CVF conference on computer vision and pattern recognition*, 2021, pp. 16 296–16 305.
- [31] R. Ding, Y. Zhou, J. Xu, Y. Xie, Q. Liang, H. Ren, Y. Wang, Y. Chen, L. Wang, and M. Huang, "Cross-hospital sepsis early detection via semi-supervised optimal transport with self-paced ensemble," *IEEE Journal of Biomedical and Health Informatics*, 2023.
- [32] H. Janati, M. Cuturi, and A. Gramfort, "Wasserstein regularization for sparse multi-task regression," in *The 22nd International Conference on Artificial Intelligence and Statistics*. PMLR, 2019, pp. 1407–1416.
- [33] P.-E. Sarlin, D. DeTone, T. Malisiewicz, and A. Rabinovich, "Superglue: Learning feature matching with graph neural networks," in *Proceedings of the IEEE/CVF conference on computer vision and pattern recognition*, 2020, pp. 4938–4947.
- [34] C. Bunne, D. Alvarez-Melis, A. Krause, and S. Jegelka, "Learning generative models across incomparable spaces," in *International conference on machine learning*. PMLR, 2019, pp. 851–861.
- [35] Z. Ge, S. Liu, Z. Li, O. Yoshie, and J. Sun, "Ota: Optimal transport assignment for object detection," in *Proceedings of the IEEE/CVF Conference on Computer Vision and Pattern Recognition*, 2021, pp. 303–312.
- [36] D. Kim and B. C. Song, "Optimal transport-based identity matching for identity-invariant facial expression recognition," *Advances in Neural Information Processing Systems*, vol. 35, pp. 18 749–18 762, 2022.
- [37] W. Zhu, P. Qiu, O. M. Dumitrascu, J. M. Sobczak, M. Farazi, Z. Yang, K. Nandakumar, and Y. Wang, "Otre: Where optimal transport guided unpaired image-to-image translation meets regularization by enhancing," in *International Conference on Information Processing in Medical Imaging*. Springer, 2023, pp. 415–427.
- [38] C. Yufei, Z. Liu, C. Yixin, Y. Lu, X. Yu, X. Liu, T.-W. Kuo, M. R. Rodrigues, C. J. Xue, and A. B. Chan, "Retrieval-augmented multiple instance learning," in *Thirty-seventh Conference on Neural Information Processing Systems*, 2023.
- [39] M. Cuturi, "Sinkhorn distances: Lightspeed computation of optimal transport," *Advances in neural information processing systems*, vol. 26, 2013.
- [40] G. Peyré, M. Cuturi *et al.*, "Computational optimal transport," *Center for Research in Economics and Statistics Working Papers*, no. 2017-86, 2017.
- [41] X. Wang, Y. Peng, L. Lu, Z. Lu, M. Bagheri, and R. M. Summers, "Chestx-ray8: Hospital-scale chest x-ray database and benchmarks on weakly-supervised classification and localization of common thorax diseases," in *Proceedings of the IEEE conference on computer vision and pattern recognition*, 2017, pp. 2097–2106.
- [42] H. Q. Nguyen, K. Lam, L. T. Le, H. H. Pham, D. Q. Tran, D. B. Nguyen, D. D. Le, C. M. Pham, H. T. Tong, D. H. Dinh *et al.*, "Vindr-cxr: An open dataset of chest x-rays with radiologist's annotations," *Scientific Data*, vol. 9, no. 1, p. 429, 2022.
- [43] G. Shih, C. C. Wu, S. S. Halabi, M. D. Kohli, L. M. Prevedello, T. S. Cook, A. Sharma, J. K. Amorosa, V. Arteaga, M. Galperin-Aizenberg *et al.*, "Augmenting the national institutes of health chest radiograph dataset with expert annotations of possible pneumonia," *Radiology: Artificial Intelligence*, vol. 1, no. 1, p. e180041, 2019.
- [44] "Society for imaging informatics in medicine: Siim-acr pneumothorax segmentation," 2019. [Online]. Available: <https://www.kaggle.com/c/siim-acr-pneumothorax-segmentation/overview/description>
- [45] X. Chen and K. He, "Exploring simple siamese representation learning," 2020.